CHEMISTRY OF MATERIALS

Open Access

This article is licensed under CC-BY-NC-ND 4.0

pubs.acs.org/cm

Article

Boron Phosphide Nanotubes for Electrocatalytic CO Reduction to Multicarbon Products

Xiaodong Yan,[#] Wugang Wang,[#] Oleg V. Prezhdo,* and Lai Xu*

Cite This: *Chem. Mater.* 2025, 37, 1382−1392

Read Online

ACCESS | Metrics & More | Article Recommendations | Supporting Information

ABSTRACT: Developing an efficient catalyst that can reduce CO to economically viable products provides a pathway to achieve carbon neutrality. For this purpose, we introduce and characterize boron phosphide nanotubes, a class of materials that allow one to reach a goal without costly and toxic metal atoms. The tubular configuration imparts a confining effect, facilitating CO adsorption and catalytic reduction into ethanol. By calculating the transition state conditions under different charging and using grand canonical potential kinetics, we establish the transition state energy barriers in the system at different electrochemical potentials. We further elucidate the kinetics and mechanism of the entire reaction process at the microkinetics level and predict the onset potential to be −0.30 V with the Tafel slope of 93.69 mV/dec. Finally, we demonstrate control over concentrations of the products and intermediate species by the choice of pH and the applied potential. The characterized material class and established chemical mechanisms guide design of electrocatalysts for producing multicarbon products.

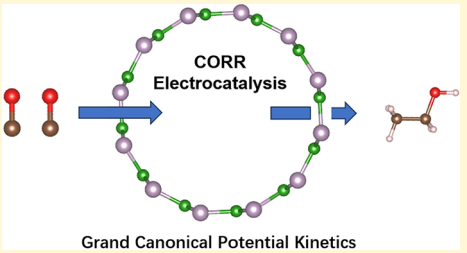

INTRODUCTION

Fossil fuels, as the primary sources of energy, have facilitated industrial development over the past few centuries. However, they have also led to excessive emissions of greenhouse gases, such as carbon dioxide, further exacerbating climate change and other global environmental issues. Reduction of carbon dioxide (CO_2) and carbon monoxide (CO) provides a promising method for converting alternative, renewable energy sources, such as solar energy, into chemical energy in the form of fuel and raw materials.[1−8] Currently, catalytic reduction of CO_2 is considered as a green and environmentally friendly approach to produce a range of multicarbon products, including carbon monoxide, methane, methanol, ethanol, and ethylene.[9−19] The process both solves the problem of carbon imbalance and generates important industrial and medical products, e.g., methane and ethanol, making it a win-win solution to the environmental and energy problems faced by modern society. However, several key challenges need to be addressed to make the catalytic reduction of CO a viable solution. The process has been limited by the high overpotential required for the CO reduction, as well as by the competitive hydrogen evolution reaction (HER), which has resulted in low production efficiency and unfavorable energy utilization.[15,20] Therefore, it is particularly important to find catalysts with high activity, stability, and selectivity.

In recent years, significant progress has been made in the reduction of CO_2 and CO.[21,22] Since the successful synthesis of graphene in 2004,[23] significant research efforts have been dedicated to two-dimensional materials, such as transition metal carbides and nitrides (MXenes)[24] and transition metal dichalcogenides (TMDCs).[25] Two-dimensional materials have a high specific surface area and are therefore promising for applications in electrochemical reactions.[26] In comparison with traditional two-dimensional planar materials, nanotubes have been proven a promising platform for promoting catalysis due to their unique tubular structure that facilitates mass diffusion, promotes charge transfer, and provides ultrahigh specific surface area.[27−29] Further, transition metal phosphides have a great potential for applications in catalysis.[30,31] Boron phosphide nanoparticles can be used for CO reduction reactions,[32] and the boron and phosphorus chemical elements can enhance the catalytic properties of materials.[33,34]

Currently, traditional quantum mechanical (QM) calculations are performed under the assumption of a fixed number of electrons, while there may be significant changes in the number of electrons during the reaction. Grand canonical quantum mechanics allows the charge to vary continuously during the calculation of the reaction properties, representing the constant applied potential experimental conditions. Formulation of the grand canonical potential kinetics (GCP-K) allows one to obtain accurate description of catalytic reactions.[35] The accuracy of the GCP-K approach has been validated in recent studies on single-crystal Co/TiO_2 nanoparticles, with the experimental results showing a close

Received: July 27, 2024
Revised: February 1, 2025
Accepted: February 3, 2025
Published: February 10, 2025

© 2025 The Authors. Published by American Chemical Society

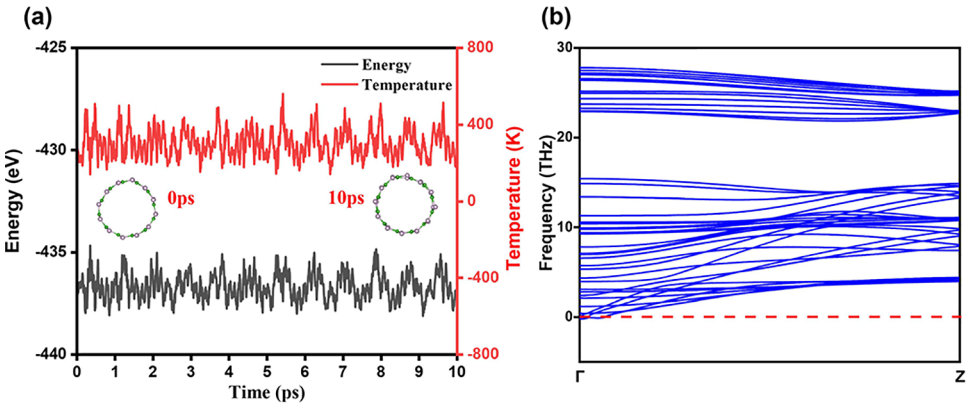

Figure 1. Stability of the BPSWNT. (a) AIMD of BPSWNT at the temperature of 300 K. Left and right coordinate axes represent temperature and energy, respectively. Initial structure of the calculation and the completed structure are shown in the illustration. (b) Phonon dispersion spectrum of BPSWNT.

agreement with the predicted relationship between turnover frequency (TOF) and applied potential, as well as the Tafel slope.[36]

In this study, we design and characterize boron phosphide nanotubes (BPSWNT), a class of materials for the catalytic reduction of CO, as illustrated in Figure S1. We demonstrate the thermodynamic and dynamic stability of the material using ab initio molecular dynamics (AIMD) and phonon spectroscopy. Leveraging the unique tubular structure of the BPSWNT, we propose a strategy to enhance the CO reduction reaction (CORR) within the confinement of the tube, thereby promoting catalytic performance. The curvature of the inner and outer walls of the tube facilitates favorable CO molecule adsorption as well as subsequent coupling and protonation steps. Employing the GCP-K approach, we report detailed microkinetic simulations, yielding an onset potential of −0.30 V and a Tafel slope of 93.69 mV/dec for the boron phosphide nanotube material at a current density of 10 mA/cm^2.

METHODS

Spin-polarized density functional theory (DFT) calculations were conducted using the Vienna ab initio simulation package (VASP), employing the Perdew−Burke−Ernzerhof (PBE) functional within the generalized gradient approximation (GGA) to describe exchange-correlation energy.[37] Electron−ion interactions were treated with the projector augmented wave (PAW) method,[38] while van der Waals interactions between atoms were considered using the DFT-D3 method with Becke−Jonson damping.[39] A plane-wave basis with a cutoff energy of 450 eV was utilized. Brillouin zone sampling was achieved employing the Gamma scheme with a 1 × 1 × 3 k-point grid for structural optimizations. Convergence thresholds for energy and forces on each atom were set to 10^{-5} eV and 0.05 eV/Å, respectively. To account for solvation effects, the VASPsol model[40] was integrated, employing a water dielectric constant of 78.50.

In this study, ab initio molecular dynamics (AIMD) simulations were conducted to evaluate the thermodynamic stability of the system. The NVT ensemble was utilized, maintaining a temperature of 300 K over a duration of 10 ps with a time step of 1 fs. Concurrently, we employed phonon spectroscopy software to simulate and assess the dynamic stability of the system. Additionally, the crystal orbital Hamiltonian population (COHP) analysis was conducted using the Lobster 4.0.0 code.[41−43] We employed the climbing-image nudged elastic band (CI-NEB) method[44] to locate the transition state (TS) and determine the reaction pathway.

Subsequently, we utilized JDFTx[45] to compute the single-point energy of the optimized structure obtained from VASP, employing the CANDLE[46] solvation model. For the single-point energy calculation in JDFTx, we employed the USPP pseudopotential, set the free energy convergence threshold to 10^{-6} Hartree, used a k-point grid of 1 × 1 × 3, specified a system cutoff energy of 15 hartree, and the spin type was designated as spin-polarized.[47]

RESULTS AND DISCUSSION

Structure. Previous studies showed that boron phosphide nanoparticles have emerged as promising catalysts.[32] In this work, we have designed boron phosphide nanotube (BPSWNT) structures by transforming two-dimensional nanosheets into tubular configurations, aiming to enhance the material's catalytic activity. The material depicted in Figure S1 consists of a B atom and a P atom. The inner radius of the tube is approximately 5.70 Å. Boron phosphide nanotubes feature a hexagonal honeycomb structure composed of boron and phosphorus atoms with an average B−P bond length of around 1.90 Å.

Boron phosphide nanotubes, composed of boron and phosphorus atoms, share structural similarities with carbon nanotubes. The inner space of these nanotubes provides space for accommodating the CO molecules and the ethanol molecules generated during the reduction reaction. Throughout the carbon monoxide reduction process, the structure of the nanotubes undergoes subtle changes as the reaction proceeds, eventually regaining its original shape after the ethanol is produced. This also indicates that phosphorus boron nanotubes have a certain degree of flexibility, allowing them to withstand certain fluctuations while maintaining their overall integrity.

To determine the stability of boron phosphide nanotubes, the thermodynamic stability of the material was explored through AIMD. Considering that electrochemical CO reduction reactions typically occur in aqueous solutions at room temperature and pressure, we simulated the energy and temperature fluctuations of the material at 300 K over a duration of 10 ps with a time step of 1 fs. Figure 1a presents the geometric structure of the material at 0 and 10 ps during AIMD, revealing minimal structural changes. This observation underscores that under room temperature conditions, boron phosphide nanotube materials maintain a stable state. In addition, phonon spectrum calculations were conducted to evaluate the dynamic stability of the material, as shown in Figure 1b. The calculation results indicate that the material has almost no imaginary frequency under the 0 scale, which provides additional evidence for the dynamic stability of the

https://doi.org/10.1021/acs.chemmater.4c02106
Chem. Mater. 2025, 37, 1382−1392

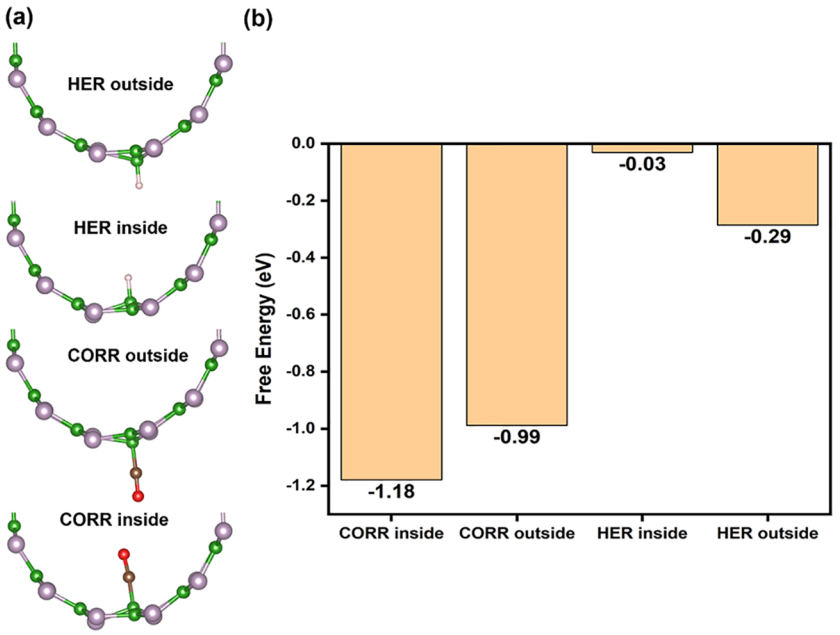

Figure 2. (a) Structures of BPSWNT with CO and H adsorbed on the inner and outer sides, respectively. (b) Free energies of the four structures in Figure 2a at 0 V.

material. In summary, these findings confirm the stability of the boron phosphide nanotubes.

CO Adsorption. Adsorption serves as a pivotal initial step in reaction pathways, and without adsorption, subsequent reactions will not occur; therefore, determining the adsorption site is crucial. Considering that the material is a repetitive tubular structure composed of boron and phosphorus atoms, two types of CO adsorption scenarios can be considered: one with single B and P atoms acting as active sites and the other with adjacent B and P atoms or two P atoms acting as a two-site mode. In the case of two-site CO adsorption, the distance between the two adsorption sites must match the length of the C−O bond. In the case of double-site CO adsorption, the distance between the two adsorption sites must match the length of the C−O bond. However, the distance between the two B or P atoms is about 2.20 Å, while the C−O bond distance in CO is about 1.14 Å, which is a large difference, thus preventing the successful adsorption of CO. Consequently, such scenarios are excluded from consideration. Subsequently, we optimized the structures for the remaining six configurations individually, as shown in Figure S2. Through calculations, it was determined that when a B atom acts as a single active site for vertical CO adsorption, successful fixation of CO onto the substrate occurs, while other configurations fail to achieve CO adsorption.

After confirmation of the CO adsorption based on B atoms, distinctions arise between the inner and outer walls of the catalyst material due to its tubular structure. Subsequently, we conducted calculations to evaluate the CO adsorption on both the inner and outer walls of the tube with B atoms as the active site. The computational results are depicted in Figure 2. Observations reveal successful CO adsorption on both surfaces; the free energy of the structure adsorbing CO inside the tube wall is −1.18 eV at an applied potential of 0 V. However, when the material adsorbs CO on the outer side, the free energy is −0.99 eV at an applied potential of 0 V, which is 0.19 eV higher than that of the inner side adsorption. This difference indicates that CO is more conducive to reaction inside the tube wall. It is worth noting that during CO adsorption, there is a significant atomic position shift on the substrate, resulting in a boron atom in the material showing a tendency to approach the adsorbed CO molecules, while adjacent phosphorus atoms shift in the opposite direction.

At the same time, we calculated the free energy of the adsorption of H on the inner and outer sides of the BPSWNT material, respectively, as shown in Figure 2. It can be found that the free energy of the material is −0.03 eV in the inner adsorption of H, which is 0.26 eV higher than that of −0.29 eV in the outer adsorption of H. However, both cases are higher than that of the material's adsorption of CO, so that the BPSWNT material is more likely to be subjected to CORR, and it can effectively inhibit the occurrence of HER.[48−50] We also calculated the free energy changes of the HER and CORR at different potentials, as shown in Figure S3. It can be observed that under an applied voltage of −0.3 V, the free energy of CORR is −1.15 eV, while that of HER is −0.43 eV, which also proves that the activity of the CORR is still superior to that of the HER at different potentials.

An insight into the electronic properties of this system can be gained by calculating the integrated crystal orbital Hamiltonian population (ICOHP) and Bader charge, as shown in Figures S4 and S5. It is worth noting that the ICOHP value of the C−O bond is highest at −9.90 eV when CO is adsorbed inside the tube. The outer adsorbed C−O bond has an ICOHP value of −9.96 eV, which is lower than the ICOHP value of the inner part of the tubular structure, which also suggests that adsorption of CO in this case presents the highest degree of activation of the C−O bonding state, and its bonding state is located at the rightmost of the two cases as proof, as shown in Figure S4. This observation indicates that the C−O bond is maximally activated in this case, achieving the best adsorption effect, confirming our early findings, as shown in Figure 2.

In addition, the study of Figure S5 reveals interesting insights into the Bader charge distribution when CO is adsorbed on the inner side of the tubular structure. It is worth

https://doi.org/10.1021/acs.chemmater.4c02106
Chem. Mater. 2025, 37, 1382−1392

noting that this configuration exhibits the lowest total Bader charge value of the CO molecule, which is −0.48 lel, lower than the −0.31 lel adsorbed on the outer side of the tubular structure, indicating that the maximum electron supply from the tubular structure to the adsorbed CO molecules can be achieved on the inner side. This difference illustrates the excellent electron supply capacity of the tubular structure, which further enhances its effectiveness in adsorbing CO.

C−C Coupling. Building upon the successful adsorption of CO, the pivotal step in generating a multicarbon product containing two carbon atoms is C−C coupling. By combining the carbon atoms from two single carbon structures are combined in a coupled form, a dual carbon product can be formed. This paper primarily focuses on the coupling step of two CO molecules, ultimately yielding COCO, from which subsequent multicarbon products are generated. Given the significance of coupling in the reaction pathway, this section specifically conducts transition state calculations on the coupling steps to further investigate the mechanism of coupling.

The coupling method considered in this paper is to adsorb a CO molecule on a B atom and then directly capture another free CO with the adsorbed CO and then couple to form COCO, which is shown in Figure S6, with a calculated transition-state barrier of 0.43 eV. From the transition state structure in Figure S6, it can be seen that the free CO initially approaches the adsorbed CO from the air, and at this time, the C−C distance between them is 3.60 Å. Then, the C atom in the two CO molecules couple, so that the free CO is captured by the adsorbed CO, and the transition state structure is formed; at this time, the C−C distance is 1.99 Å. After the C−C coupling to form COCO, the C atom is finally adsorbed by the P atom of the neighboring B atom. Finally, the boron and phosphorus nanotubes adsorb the two C atoms of COCO onto the neighboring boron and phosphorus atoms, completing the reaction step with a C−C distance of 1.59 Å.

At the same time, we also considered the addition of more H to the reaction environment, as shown in Figures S7 and S8. It can be seen that in the path calculations under two H environments, the highest required energy is −0.60 eV, and then, the highest energy required for H to react with intermediates is −0.71 eV, indicating that it is more likely to occur. Further, our calculations indicate that the interaction between H and CO−CO coupling intermediates is better than that between H and the material, as shown in Figure S9.

Following the discussion of adsorption and coupling reactions above, we performed transition state search calculations for the subsequent 8-electron pathway to the C_2 product ethanol (CH_3CH_2OH) over boron phosphide nanotube catalysts. The transition state barriers for the subsequent hydrogenation and protonation steps are all close to zero, except for the hydrogenation of $*CH_3COH$ to $*CH_3CHOH$, which has a higher transition state barrier of 0.42 eV. The main reason for the generation of the high-energy barrier is the change in the reaction site, the C atom on the substrate of the CH_3COH linkage is in a tetra-coordinated state, and the reaction site needs to be reduced by one to provide a position for the H in the process of hydrogenation, as shown in Figure S10. Also, Figures S11−S16 show the structure of the initial, transition, and final states with transition state energy barrier close to 0.

Grand Canonical DFT Calculation. At the same time, we also carried out calculations for the transition states with different charges and listed the change of the transition states with different charges for the steps with higher energy barriers, as shown in Figures S17−S18. From the figures, it can be found that for the transition state energy barriers of different steps, the effects of different charges on them are different, the step of coupling has a smaller change for the charge effect, and the transition state energy barriers are almost similar to the change of charge, which basically remains at 0.43 eV from −0.25 to 0.25 e. For the step of $*CH_3COH$ hydrogenation to $*CH_3CHOH$, the transition state energy barrier is affected by the change of charge, as shown in Figure S14, the transition state energy barrier is more affected by the charge, and in the case of going from −0.25 to 0.10 e, the transition state energy barrier decreases from 0.49 to 0.40 eV. In the discussion above, the transition state energy barrier of the coupling is the highest in the case of zero charge. However, from the calculations of different charges, it can be found that in the case of −0.25 e, the $*CH_3COH$ hydrogenation is 0.06 eV higher than the transition state barrier of the coupling step. The transition state barrier of $*CH_3COH$ hydrogenation is 0.03 eV lower than the transition state barrier of the coupling step at 0.10 e. Therefore, the study of the situation at different charges can be beneficial to a more in-depth understanding of the reaction mechanism of the catalytic process.

In order to further investigate the effect of different charges on the transition state, we plotted the effect of charge on the structural change of the transition state, as shown in Figure S19. O−H bond distance versus net charge change for the transition state structure of *CO*COH hydrogenated to generate *COH*COH. It can be found that for the transition state for the hydrogenation of COCOH to generate COHCOH, its O−H bonding distance changes from 2.72 to 2.67 Å in the range of charge change from 0 to 1 e, which is a shortening of the distance by 0.05 Å. This also indicates that the bonding distance required for the transition state decreases gradually with the increase of charge, which means that the reaction gets closer to the product and vice versa to the reactant.

In traditional density functional theory (DFT), it typically employs a fixed number of electrons. However, real experimental responses tend to keep the potential constant.[35] In our study, we introduced GCP (U) to consider electronic changes of the system by establishing an invariant potential, thereby obtaining a more realistic representation of catalytic reactions. Initially, we optimized the structure of systems with different charges by using VASP software. Subsequently, we derived the free energy of the system using the JDFT method[45] for grand canonical DFT energy calculations under the CANDLE[46] implicit solvent model conditions.

Recently, the grand canonical potential kinetics (GCP-K) methodology has been developed to characterize the change in response with an applied potential as the independent variable.[51] GCP-K transforms $F(n)$, which describes the free energy in terms of charge as a variable, into $G(n; U)$ in terms of applied potential and charge by means of the Legendre transformation, which is defined as[52,53]

$$G(n; U) = F(n) - ne(U_{SHE} - U) \quad ((1))$$

where G is the grand canonical potential free energy, which is obtained from the function $F(n)$ describing the total free energy in terms of charge as a variable, the number of electrons (n), the energy of the electrons

https://doi.org/10.1021/acs.chemmater.4c02106
Chem. Mater. 2025, 37, 1382−1392

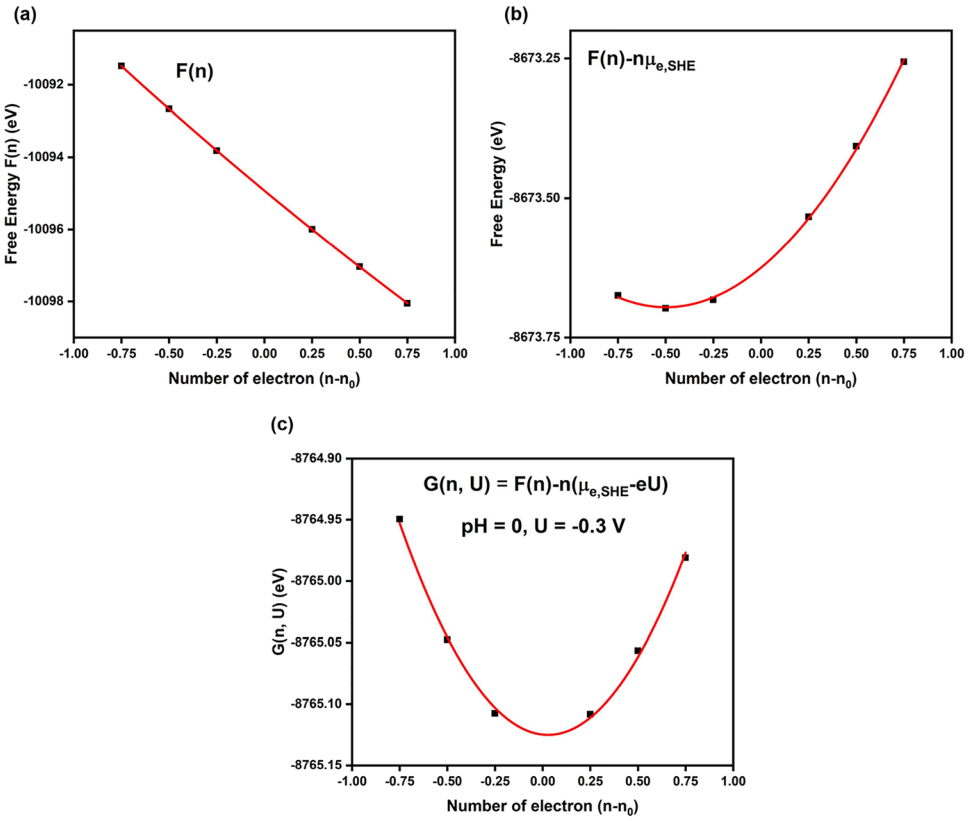

Figure 3. Relationship between free energy and net electron number of the structure of *CH_2COH in BPSWNT under the grand canonical potential. (a) Relationship between total free energy and the net number of electrons. (b) Relationship between free energy and the net number of electrons after removing electron contributions under standard hydrogen electrode (SHE) conditions. (c) Relationship between free energy and net electron number obtained by increasing the potential to −0.30 V.

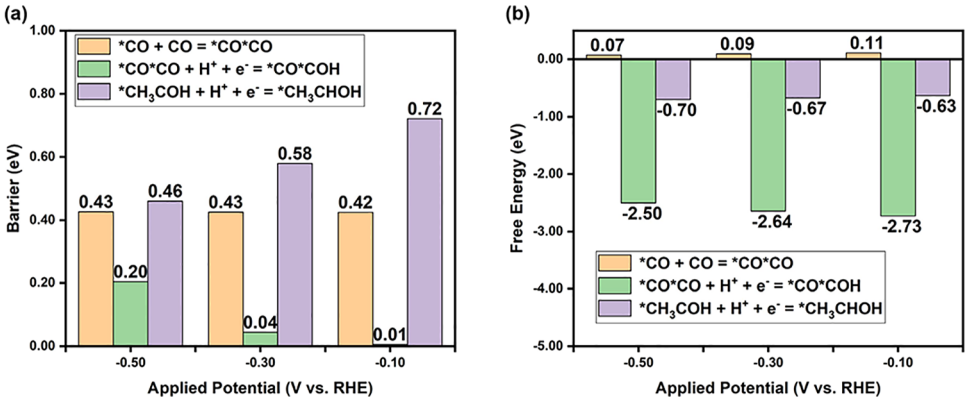

Figure 4. Reaction (a) transition state energy barriers and (b) free energy of FS-IS for the three key steps of C−C coupling to generate *CO*CO, *CO*CO hydrogenation to achieve *CO*COH and *CH_3COH hydrogenation to generate *CH_3CHOH in BPSWNT at pH = 0 under applied voltages of −0.10, −0.30, and −0.50 V.

$\left(U_{\mathrm{SHE}} = \frac{\mu_{e,\mathrm{SHE}}}{e}, \mu_{e,\mathrm{SHE}} = -4.66\ \mathrm{eV}\right)$ at the standard hydrogen electrode (SHE), and the applied potential (U vs SHE). In order for G to be described by an applied potential, *this would require* matching the electron Fermi energy level with the energy level of the applied potential by varying the occupation of the electron band and thus the number of electrons.[46] And that means

$$\frac{dG(n;U)}{dn} = 0 \text{ or } \frac{dF(n)}{dn} = e(U_{\mathrm{SHE}} - U) \quad ((2))$$

Therefore, according to formulas S21−S23, the grand canonical potential as a function of U can be defined *as*

$$\mathrm{GCP}(U) = \min_n G(n;U) = \min_n [F(n) - ne(U_{\mathrm{SHE}} - U)]$$
$$= -\frac{1}{4a}(b - \mu_{e,\mathrm{SHE}} + eU)^2 + c - n_0\mu_{e,\mathrm{SHE}} + n_0\, eU \quad ((3))$$

Following these calculations, we observed a linear relationship between the reaction free energy $F(n)$ obtained through the JDFT method and the net charge of the system, as shown in Figure 3a. Subsequently, by subtracting the contribution of

https://doi.org/10.1021/acs.chemmater.4c02106
Chem. Mater. 2025, 37, 1382−1392

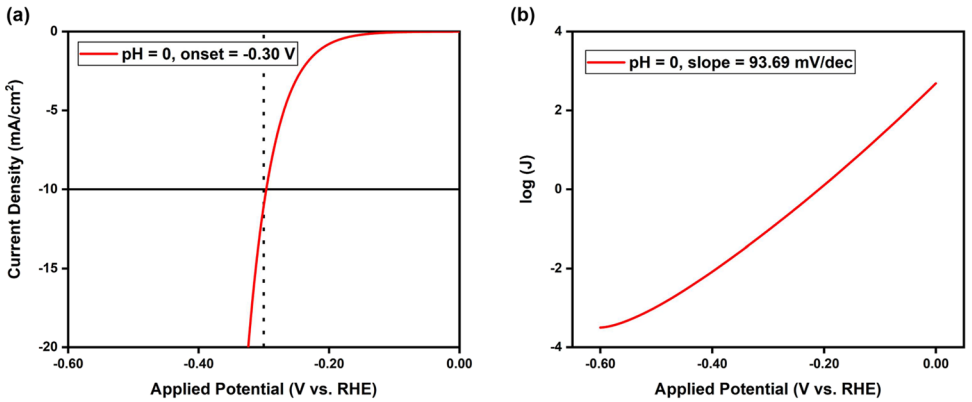

Figure 5. (a) Relationship between applied potential and current density of BPSWNT under acidic conditions. (b) Corresponding Tafel curve.

each electron at the standard hydrogen electrode (SHE), a plot of the corrected free energy against the net charge of the system was constructed, as shown in Figure 3b. It can be found that the free energy of the system at this point is quadratically related to the net charge. The minimum value of free energy is at −0.50 e net charge, which reduces it by 0.44 eV compared to the free energy at 0.75 e net charge. Lastly, the reaction continues to occur and proceeds under an external potential. As shown in Figure 3c, $G(n)$ also exhibits a quadratic relationship with net charge. At this point, the lowest point of the quadratic function is located near the 0 net charge, which is shifted to the right by 0.50 e net charge compared to the case without an applied potential, which also indicates that for the $*CH_2COH$ intermediate, the application of an external potential of −0.30 V is equivalent to an increase of the system by approximately 0.50 e net charge. At the same time, it can be noticed that the quadratic relationship between energy and charge in the system is enhanced and made more pronounced with the introduction of the applied potential.

By fitting the relationship between the free energy and charge of the system, we obtained the corresponding parameters a, b, and c for each intermediate species, as shown in Tables S1−S3. Using these parameters, we established the relationship between the applied potential and energy. After completing the calculation of intermediates, we also performed corresponding calculations on the transition states of each step in the entire reaction and obtained similar patterns. We have listed in Figure 4 the free energy and transition state barriers of key steps under applied potentials of −0.10, −0.30, and −0.50 V. It can be observed that the influence of the transition state barrier of the coupling step on the potential change is relatively small. With the increase of the applied potential, the transition state barrier basically remains at 0.43 eV, but the free energy will decrease under the influence of potential, from the original 0.11 to 0.07 eV. At potential of −0.10 V, the highest energy barrier step is the step of $*CH_3COH$ hydrogenation to generate $*CH_3CHOH$, it is greatly affected by potential changes, and as the applied potential is more negative, its transition state energy barrier will decrease from 0.72 to 0.46 eV.

All of the intermediates and transition state free energies in the reactions are calculated using the quadratic transformation of the energy obtained through grand canonical calculations. Given that the reaction rate for each step is directly influenced by the applied potential, we derived rate equations to understand the variation rates at each step of the reaction. Finally, we established a microkinetic model to obtain the overall reaction rate and concentrations. The rate equation for each intermediate state in the reaction is shown in formulas S1−S10 in the Supporting Information.

Microkinetics. The Eyring rate equation is used to express the rate constant of a chemical reaction and is given by the following expression: $k = \frac{k_B T}{h} e^{-\Delta G/k_B T}$. Among them, k_B is the Boltzmann constant, h is the Planck constant, T is the reaction temperature (room temperature = 298.15 K), and ΔG is the energy barrier for each transition state of the reaction. x_i represents the concentration of each species in the reaction, and we have established constraint conditions $\sum_i x_i = 1$. At the same time, because we are considering steady-state conditions, the left side of the above rate equation is 0, so we can solve for the species concentration in each step of the reaction. By solving the above equation, we obtained the reaction rates of each intermediate state in the total reaction under steady-state approximation conditions. We ultimately derived the function of the current density variation with applied external potential, represented as the $I-V$ curve and Tafel slope plot, as shown in Figure 5. From the graph, it is observed that at a current density of 10 mA/cm^2, the onset potential of the system is −0.30 V, with a corresponding Tafel slope of 93.69 mV/dec.

Meanwhile, as shown in Tables S4 and S5, we listed the relevant values of the onset potential and Tafel slope for electrocatalytic reduction of CO or CO_2 with other materials, thus illustrating the superior performance of the BPSWNT material for the electrocatalytic reduction reaction. The onset potential of the BPSWNT material was −0.30 eV, the Tafel slope was 93.69 mV/dec, and both the onset potential and the Tafel slope of BPSWNT are better than most of the current electrocatalysts.

We plotted Figure 6 to obtain the concentration of species at a key step of the reaction at different potentials. As seen from Figure 6, the highest concentration of intermediate structures in $*CH_3COH$ was observed under low potential conditions. It can also be seen from Figure 4 that the hydrogenation of $*CH_3COH$ is the highest energy barrier to be crossed among all the intermediates, under 0 to −0.30 V applied potential conditions. As a result, at an applied potential of 0 V, the highest concentration fraction of the $*CH_3COH$ intermediate is close to 1 and the concentration fractions of the other intermediates are near 0. Then, when the applied potential reaches the onset potential of −0.30 V, the reaction starts to proceed and the concentration fractions of the other intermediates begin to increase. Because the energy barrier of the coupling step is less affected with potential and basically

https://doi.org/10.1021/acs.chemmater.4c02106
Chem. Mater. 2025, 37, 1382−1392

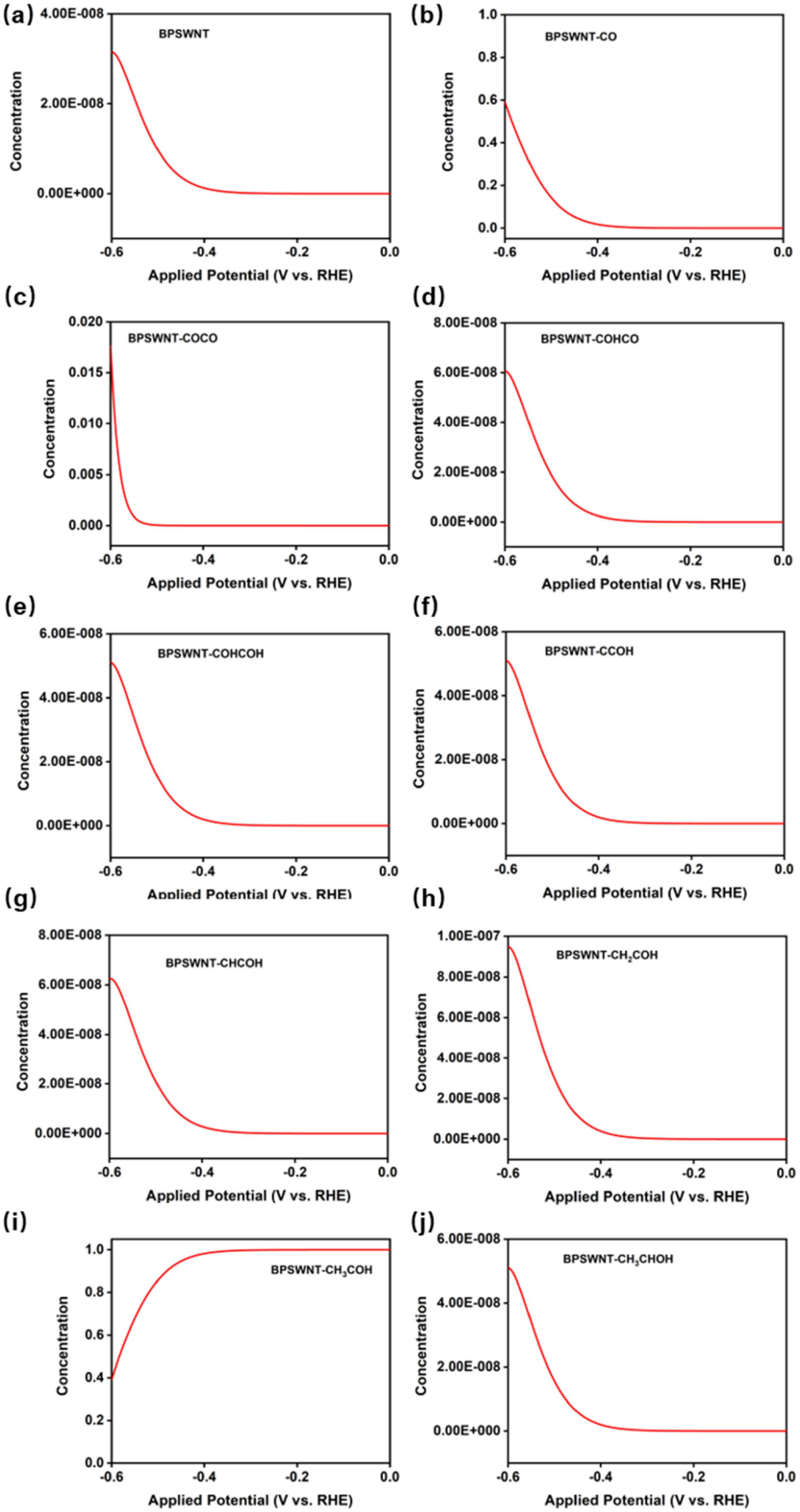

Figure 6. Changes in the concentration components of reaction intermediates at different potentials at pH = 0 (concentrations normalized to 1).

stays at 0.43 eV and the energy barrier of the *CH_3COH hydrogenation step is greatly affected by potential, the *CO concentration starts to increase at an applied potential of −0.43 V. It can be found that at an applied potential of −0.60

https://doi.org/10.1021/acs.chemmater.4c02106
Chem. Mater. 2025, 37, 1382−1392

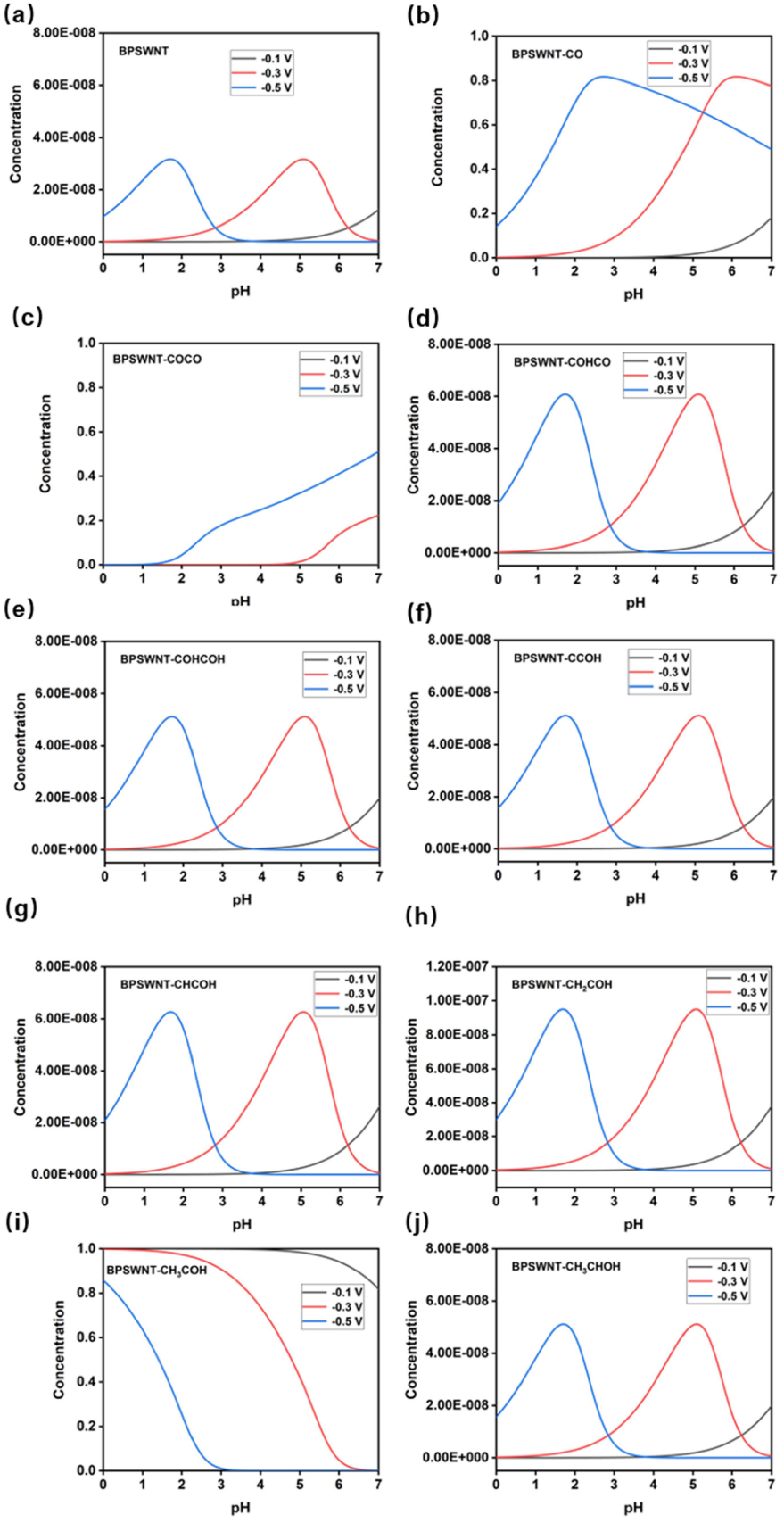

Figure 7. Changes in the concentration composition of reaction intermediates (concentration normalized to 1) at different pH values with applied potentials of −0.10, −0.30, and −0.50 V.

https://doi.org/10.1021/acs.chemmater.4c02106
Chem. Mater. 2025, 37, 1382−1392

V, the *CO intermediate has become the main component. *CO intermediate has become the main component with a concentration of 59%, and the concentration component of BPSWNT-CH_3COH intermediate decreases from 100% to 39%.

From Figure 7, it can be found that at an applied potential of −0.10 V, there is almost no change in the intermediate species except that the concentration starts to change when approaching the neutral condition. This is because it can be found in Figure S20 that at −0.10 V applied potential at pH = 3.50, the energy barrier for the hydrogenation of *CH_3COH still remains the highest at 0.57 eV, so the concentration of *CH_3COH intermediate has been dominant and close to 1. At pH 7, the energy barrier for the hydrogenation of *CH_3COH to form *CH_3CHOH is 0.45 eV, and the coupling energy barrier is 0.43 eV, so the *CH_3COH intermediate no longer dominates and the CO intermediate fraction starts to increase, but since it is still 0.02 eV lower, the *CH_3COH and *CO concentrations are 82% and 18%, respectively, at pH = 7.

When the applied potential reaches −0.30 V, it can be found that at pH = 0, the energy barrier of *CH_3COH hydrogenation stays the highest at 0.58 eV in Figure S21, so the concentration fraction of *CH_3COH is close to 1. At a pH of 3.5 and an applied voltage of −0.30 V, the energy barrier of *CH_3COH hydrogenation is still the highest at 0.46 eV, but the coupling barrier is just lower by 0.03 eV, so the *CO intermediate component starts to increase to 16%. When pH is 7, the energy barrier of *CH_3COH hydrogenation becomes 0.36 eV, the coupling energy barrier is 0.43 eV, and the hydrogenation energy barrier after coupling is 0.51 eV. So, *CH_3COH intermediate component decreases, and the concentration components of *CO and *COCO intermediates increase, which are 78% and 22%, respectively.

When the applied potential reaches −0.50 V, at pH = 0, the coupling energy barrier is close to that of CH_3COH hydrogenation to produce CH_3CHOH, which is 0.43 and 0.46 eV, respectively, as shown in Figure S22. CH_3COH intermediate no longer directly dominates as before, and its concentration fraction is 86%. When the pH is 3.50, its transition state energy barrier of 0.36 eV has been the smallest of the three key transition state energy barriers, so its concentration component in this interval decreases rapidly. The energy barrier of hydrogenation after coupling is 0.07 eV higher than the coupling energy barrier, so the concentration of *CO intermediate begins to decline and the concentration of *COCO intermediate begins to rise. Until pH = 7, *CO and *COCO intermediates together occupy the main position, and the concentration components are 49% and 51%, respectively.

In the meantime, we also considered the possibility of generating C1 and C2 products. For the C1 product, we considered CO hydrogenation to form COH and CHO, and we determined that the BPSWNT material is more likely to produce CHO. The energy required to produce COH is higher than that for the rate-determining step of the C2 pathway. On this basis, we calculated the free energy of each reaction step in the subsequent generation of CH_4 products, as shown in Figure S23. We also calculated the transition states of the CO hydrogenation to generate CHO and the transition states of the CHO and CO coupling, as shown in Figure S24. These energy barriers at zero charge are 2.18 and 1.06 eV, respectively, while the transition state energy barrier for the CO−CO coupling is 0.43 eV. This indicates that the two CO couplings are more likely to occur, proving that for BPSWNT materials, C2 reactions are more favorable.

On this basis, we also considered ethylene and calculated its path structure free energies, as shown in Figure S25. We find that ethylene can adsorb on the substrate, while ethanol cannot adsorb on the substrate and will be directly desorbed, as shown in Figure S26. This also indicates that for BPSWNT materials, producing ethylene is more difficult than producing ethanol. Therefore, this article mainly discusses the reaction pathway for producing ethanol. Similarly, we calculated alternative pathways for generating ethanol and considered using *C*CO instead of *COH*COH to generate *C*COH, as shown in Figure S27. The energy required to generate *C*COH through *COH*COH is −0.95 eV, and the energy required to generate *C*COH through *C*CO is −0.66 eV. Therefore, *COH*COH is more easily formed. Hence, we adopt the current pathway to generate ethanol.

CONCLUSIONS

In summary, we have designed a boron phosphide nanotube material for catalytic CO reduction reactions. The thermodynamic and dynamic stability of the material has been confirmed through ab initio molecular dynamics and phonon spectroscopy, demonstrating feasibility for experimental synthesis. Subsequently, we have reported an extensive investigation of the electronic characteristics of CO adsorption on the tubular structure. Our results show that the material is able to adsorb CO more easily on the inner side by utilizing the confinement effect unique to its tubular structure, which improves the adsorption performance. Subsequently, we characterized the coupling methodology of the material, ultimately identifying the optimal coupling approach. Lastly, we have established the reaction mechanism and kinetics of boron phosphide nanotubes in CO reduction reactions using a grand canonical potential kinetic approach (GCP-K). Through this method, we have predicted that the onset potential of the material for the CORR is −0.30 V, and the Tafel slope is 93.69 mV/dec. We have demonstrated control over the reaction step barriers, free energies, and concentration of reaction intermediates by the applied potential and pH value. The designed material is efficient and stable, providing a promising route to electrochemical CO reduction and related chemical processes.

ASSOCIATED CONTENT

Supporting Information

The Supporting Information is available free of charge at https://pubs.acs.org/doi/10.1021/acs.chemmater.4c02106.

Structural information, computational methods, adsorption pattern, crystal orbital Hamilton population analyses, Bader charge, energy barrier diagrams, reaction equations, rate equations, fitted parameters of the grand canonical potential or free energy for BPSWNT, comparison with other catalysts, and changes in the concentration components (PDF)

AUTHOR INFORMATION

Corresponding Authors

Oleg V. Prezhdo − *Department of Chemistry, University of Southern California, Los Angeles, California 90089, United States;* orcid.org/0000-0002-5140-7500; Email: prezhdo@usc.edu

https://doi.org/10.1021/acs.chemmater.4c02106
Chem. Mater. 2025, 37, 1382−1392

Lai Xu − *Institute of Functional Nano & Soft Materials (FUNSOM), Jiangsu Key Laboratory of Advanced Negative Carbon Technologies, Jiangsu Key Laboratory for Carbon-Based Functional Materials & Devices, Joint International Research Laboratory of Carbon-Based Functional Materials and Devices, Soochow University, Suzhou 215123 Jiangsu, PR China*; orcid.org/0000-0003-2473-3359; Email: xulai15@suda.edu.cn

Authors

Xiaodong Yan − *Institute of Functional Nano & Soft Materials (FUNSOM), Jiangsu Key Laboratory of Advanced Negative Carbon Technologies, Jiangsu Key Laboratory for Carbon-Based Functional Materials & Devices, Joint International Research Laboratory of Carbon-Based Functional Materials and Devices, Soochow University, Suzhou 215123 Jiangsu, PR China*

Wugang Wang − *Institute of Functional Nano & Soft Materials (FUNSOM), Jiangsu Key Laboratory of Advanced Negative Carbon Technologies, Jiangsu Key Laboratory for Carbon-Based Functional Materials & Devices, Joint International Research Laboratory of Carbon-Based Functional Materials and Devices, Soochow University, Suzhou 215123 Jiangsu, PR China*

Complete contact information is available at: https://pubs.acs.org/10.1021/acs.chemmater.4c02106

Author Contributions

#X.Y. and W.W. contributed equally to this work.

Notes

The authors declare no competing financial interest.

■ ACKNOWLEDGMENTS

L.X. acknowledges financial support from National Natural Science Foundation of China-General Program (22273063), Major Program in Jiangsu University Natural Science Research (21KJA150004), Suzhou Technology Innovation Policy Independent Program, Suzhou Key Laboratory of Functional Nano & Soft Materials, Collaborative Innovation Center of Suzhou Nano Science & Technology, and the 111 Project. O.V.P. acknowledges support of the US National Science Foundation (CHE-2154367).

■ REFERENCES

(1) Luo, W.; Nie, X.; Janik, M. J.; Asthagiri, A. Facet dependence of CO_2 reduction paths on Cu electrodes. *ACS Catal.* **2016**, *6* (1), 219−229.

(2) Das, A.; Mandal, S. C.; Pathak, B. Organic additive for the selective C_2-product formation on Cu(100): a density functional theory mechanistic study. *Catal. Sci. Technol.* **2023**, *13* (18), 5365−5373.

(3) Bagchi, D.; Riyaz, M.; Raj, J.; Roy, S.; Singh, A. K.; Cherevotan, A.; Vinod, C. P.; Peter, S. C. Unraveling the cooperative mechanisms in ultralow copper-loaded WC@NGC for enhanced CO_2 electroreduction to acetic acid. *Chem. Mater.* **2024**, *36* (7), 3464−3476.

(4) Vichou, E.; Perazio, A.; Adjez, Y.; Gomez-Mingot, M.; Schreiber, M. W.; Sánchez-Sánchez, C. M.; Fontecave, M. Tuning selectivity of acidic carbon dioxide electrolysis via surface modification. *Chem. Mater.* **2023**, *35* (17), 7060−7068.

(5) Feld, L. G.; Boehme, S. C.; Morad, V.; Sahin, Y.; Kaul, C. J.; Dirin, D. N.; Raino, G.; Kovalenko, M. V. Quantifying forster resonance energy transfer from single perovskite quantum dots to organic dyes. *ACS Nano* **2024**, *18* (14), 9997−10007.

(6) Arenas Esteban, D.; Pacquets, L.; Choukroun, D.; Hoekx, S.; Kadu, A. A.; Schalck, J.; Daems, N.; Breugelmans, T.; Bals, S. 3D characterization of the structural transformation undergone by Cu@Ag core−shell nanoparticles following CO_2 reduction reaction. *Chem. Mater.* **2023**, *35* (17), 6682−6691.

(7) Vos, R. l E.; Kolmeijer, K. E.; Jacobs, T. S.; van der Stam, W.; Weckhuysen, B. M.; Koper, M. T. M. How temperature affects the selectivity of the electrochemical CO_2 reduction on copper. *ACS Catal.* **2023**, *13* (12), 8080−8091.

(8) Pham, T. H. M.; Zhang, J.; Li, M.; Shen, T.-H.; Ko, Y.; Tileli, V.; Luo, W.; Zuttel, A. Enhanced electrocatalytic CO_2 reduction to C_{2+} products by adjusting the local reaction environment with polymer binders. *Adv. Energy Mater.* **2022**, *12* (9), No. 2103663.

(9) Gao, D.; Arán-Ais, R. M.; Jeon, H. S.; Roldan Cuenya, B. Rational catalyst and electrolyte design for CO_2 electroreduction towards multicarbon products. *Nat. Catal.* **2019**, *2* (3), 198−210.

(10) Gauthier, J. A.; Lin, Z.; Head-Gordon, M.; Bell, A. T. Pathways for the Formation of C2+ Products under Alkaline Conditions during the Electrochemical Reduction of CO2. *ACS Energy Letters* **2022**, *7* (5), 1679−1686.

(11) Mandal, S. C.; Das, A.; Roy, D.; Das, S.; Nair, A. S.; Pathak, B. Developments of the heterogeneous and homogeneous CO_2 hydrogenation to value-added C_{2+}-based hydrocarbons and oxygenated products. *Coordin. Chem. Rev.* **2022**, *471*, No. 214737.

(12) Garza, A. J.; Bell, A. T.; Head-Gordon, M. Mechanism of CO_2 reduction at copper surfaces: pathways to C_2 products. *ACS Catal.* **2018**, *8* (2), 1490−1499.

(13) Liu, X.; Schlexer, P.; Xiao, J.; Ji, Y.; Wang, L.; Sandberg, R. B.; Tang, M.; Brown, K. S.; Peng, H.; Ringe, S.; Hahn, C.; Jaramillo, T. F.; Norskov, J. K.; Chan, K. pH effects on the electrochemical reduction of CO_2 towards C_2 products on stepped copper. *Nat. Commun.* **2019**, *10* (1), 32.

(14) Das, A.; Mandal, S. C.; Das, S.; Pathak, B. Ga and Zn atom-doped $CuAl_2O_4$(111) surface-catalyzed CO_2 conversion to dimethyl ether: Importance of acidic sites. *J. Phys. Chem. C* **2022**, *126* (51), 21628−21637.

(15) Kortlever, R.; Shen, J.; Schouten, K. J.; Calle-Vallejo, F.; Koper, M. T. Catalysts and reaction pathways for the electrochemical reduction of carbon dioxide. *J. Phys. Chem. Lett.* **2015**, *6* (20), 4073−4082.

(16) Li, F.; Thevenon, A.; Rosas-Hernandez, A.; Wang, Z.; Li, Y.; Gabardo, C. M.; Ozden, A.; Dinh, C. T.; Li, J.; Wang, Y.; Edwards, J. P.; Xu, Y.; McCallum, C.; Tao, L.; Liang, Z. Q.; Luo, M.; Wang, X.; Li, H.; O'Brien, C. P.; Tan, C. S.; Nam, D. H.; Quintero-Bermudez, R.; Zhuang, T. T.; Li, Y. C.; Han, Z.; Britt, R. D.; Sinton, D.; Agapie, T.; Peters, J. C.; Sargent, E. H. Molecular tuning of CO_2-to-ethylene conversion. *Nature* **2020**, *577* (7791), 509−513.

(17) Chen, X.; Chen, J.; Alghoraibi, N. M.; Henckel, D. A.; Zhang, R.; Nwabara, U. O.; Madsen, K. E.; Kenis, P. J. A.; Zimmerman, S. C.; Gewirth, A. A. Electrochemical CO_2-to-ethylene conversion on polyamine-incorporated Cu electrodes. *Nat. Catal.* **2021**, *4* (1), 20−27.

(18) Wang, Z.; Li, Y.; Zhao, X.; Chen, S.; Nian, Q.; Luo, X.; Fan, J.; Ruan, D.; Xiong, B. Q.; Ren, X. Localized alkaline environment via In situ electrostatic confinement for enhanced CO_2-to-ethylene conversion in neutral medium. *J. Am. Chem. Soc.* **2023**, *145* (11), 6339−6348.

(19) Hoang, T. T. H.; Verma, S.; Ma, S.; Fister, T. T.; Timoshenko, J.; Frenkel, A. I.; Kenis, P. J. A.; Gewirth, A. A. Nanoporous copper-silver alloys by additive-controlled electrodeposition for the selective electroreduction of CO_2 to ethylene and ethanol. *J. Am. Chem. Soc.* **2018**, *140* (17), 5791−5797.

(20) Clark, E. L.; Hahn, C.; Jaramillo, T. F.; Bell, A. T. Electrochemical CO_2 reduction over compressively strained CuAg surface alloys with enhanced multi-carbon oxygenate selectivity. *J. Am. Chem. Soc.* **2017**, *139* (44), 15848−15857.

(21) Woldu, A. R.; Huang, Z.; Zhao, P.; Hu, L.; Astruc, D. Electrochemical CO_2 reduction (CO_2RR) to multi-carbon products

over copper-based catalysts. *Coord. Chem. Rev.* **2022**, *454*, No. 214340.
(22) Amirbeigiarab, R.; Tian, J.; Herzog, A.; Qiu, C.; Bergmann, A.; Cuenya, B. R.; Magnussen, O. M. Atomic-scale surface restructuring of copper electrodes under CO_2 electroreduction conditions. *Nat. Catal.* **2023**, *6* (9), 837−846.
(23) Novoselov, K. S.; Geim, A. K.; Morozov, S. V.; Jiang, D.; Zhang, Y.; Dubonos, S. V.; Grigorieva, I. V.; Firsov, A. A. Electric field effect in atomically thin carbon films. *Science* **2004**, *306* (5696), 666−669.
(24) Meng, L.; Yan, L.-K.; Vines, F.; Illas, F. Surface termination dependent carbon dioxide reduction reaction on Ti_3C_2 MXene. *J. Mater. Chem. A* **2024**, *12* (13), 7856−7874.
(25) Li, Z.; Attanayake, N. H.; Blackburn, J. L.; Miller, E. M. Carbon dioxide and nitrogen reduction reactions using 2D transition metal dichalcogenide (TMDC) and carbide/nitride (MXene) catalysts. *Energy Environ. Sci.* **2021**, *14* (12), 6242−6286.
(26) Chia, X.; Pumera, M. Characteristics and performance of two-dimensional materials for electrocatalysis. *Nat. Catal.* **2018**, *1* (12), 909−921.
(27) Zhao, R.; Wang, Y.; Ji, G.; Zhong, J.; Zhang, F.; Chen, M.; Tong, S.; Wang, P.; Wu, Z.; Han, B.; Liu, Z. Partially nitrided Ni nanoclusters achieve energy-efficient electrocatalytic CO_2 reduction to CO at ultralow overpotential. *Adv. Mater.* **2023**, *35* (5), No. 2205262.
(28) Fan, K.; Jia, Y.; Ji, Y.; Kuang, P.; Zhu, B.; Liu, X.; Yu, J. Curved surface boosts electrochemical CO_2 reduction to formate via bismuth nanotubes in a wide potential window. *ACS Catal.* **2020**, *10* (1), 358−364.
(29) Chaipornchalerm, P.; Nunthakitgoson, W.; Mano, P.; Kidkhunthod, P.; Montoya, A.; Namuangruk, S.; Wattanakit, C. Rational design of Fe single sites supported on hierarchical zeolites via atomic layer deposition for few-walled carbon nanotube production. *ACS Appl. Mater. Interfaces.* **2024**, *16* (26), 33590−33600.
(30) Pu, Z.; Liu, T.; Amiinu, I. S.; Cheng, R.; Wang, P.; Zhang, C.; Ji, P.; Hu, W.; Liu, J.; Mu, S. Transition-metal phosphides: Activity origin, energy-related electrocatalysis applications, and synthetic strategies. *Adv. Funct. Mater.* **2020**, *30* (45), No. 2004009.
(31) Batugedara, T. N.; Brock, S. L. Role of noble- and base-metal speciation and surface segregation in $Ni_{2-x}Rh_xP$ nanocrystals on electrocatalytic water splitting reactions in alkaline media. *Chem. Mater.* **2022**, *34* (10), 4414−4427.
(32) Mou, S.; Wu, T.; Xie, J.; Zhang, Y.; Ji, L.; Huang, H.; Wang, T.; Luo, Y.; Xiong, X.; Tang, B.; Sun, X. Boron phosphide nanoparticles: A nonmetal catalyst for high-selectivity electrochemical reduction of CO_2 to CH_3OH. *Adv. Mater.* **2019**, *31* (36), No. 1903499.
(33) Hussien, M. K.; Sabbah, A.; Qorbani, M.; Putikam, R.; Kholimatussadiah, S.; Tzou, D. M.; Elsayed, M. H.; Lu, Y. J.; Wang, Y. Y.; Lee, X. H.; Lin, T. Y.; Thang, N. Q.; Wu, H. L.; Haw, S. C.; Wu, K. C.; Lin, M. C.; Chen, K. H.; Chen, L. C. Constructing B-N-P Bonds in ultrathin holey g-C_3N_4 for regulating the local chemical environment in photocatalytic CO_2 reduction to CO. *Small* **2024**, *20* (35), No. 2400724.
(34) Song, J.; Lei, X.; Mu, J.; Li, J.; Song, X.; Yan, L.; Ding, Y. Boron-doped nickel-nitrogen-carbon single-atom catalyst for boosting electrochemical CO_2 reduction. *Small* **2023**, *19* (52), No. 2305666.
(35) Sundararaman, R.; Goddard, W. A.; Arias, T. A. Grand canonical electronic density-functional theory: Algorithms and applications to electrochemistry. *J. Chem. Phys.* **2017**, *146* (11), 114104.
(36) Liu, C.; Qian, J.; Ye, Y.; Zhou, H.; Sun, C.-J.; Sheehan, C.; Zhang, Z.; Wan, G.; Liu, Y.-S.; Guo, J.; Li, S.; Shin, H.; Hwang, S.; Gunnoe, T. B.; Goddard, W. A., III; Zhang, S. Oxygen evolution reaction over catalytic single-site Co in a well-defined brookite TiO_2 nanorod surface. *Nat. Catal.* **2021**, *4* (1), 36−45.
(37) Perdew, J. P.; Burke, K.; Ernzerhof, M. Generalized gradient approximation made simple. *Phys. Rev. Lett.* **1997**, *78* (7), 1396−1396.
(38) Blochl, P. E. Projector augmented-wave method. *Phys. Rev. B* **1994**, *50* (24), 17953−17979.
(39) Grimme, S.; Antony, J.; Ehrlich, S.; Krieg, H. A consistent and accurate ab initio parametrization of density functional dispersion correction (DFT-D) for the 94 elements H-Pu. *J. Chem. Phys.* **2010**, *132* (15), 154104.
(40) Mathew, K.; Sundararaman, R.; Letchworth-Weaver, K.; Arias, T. A.; Hennig, R. G. Implicit solvation model for density-functional study of nanocrystal surfaces and reaction pathways. *J. Chem. Phys.* **2014**, *140* (8), No. 084106.
(41) Dronskowski, R.; Blochl, P. E. Crystal orbital hamilton populations (COHP) - energy-resolved visualization of chemical bonding in solids based on density-functional calculations. *J. Phys. Chem. C* **1993**, *97* (33), 8617−8624.
(42) Maintz, S.; Deringer, V. L.; Tchougréeff, A. L.; Dronskowski, R. LOBSTER: A tool to extract chemical bonding from plane-wave based DFT. *J. Comput. Chem.* **2016**, *37* (11), 1030−1035.
(43) Deringer, V. L.; Tchougreeff, A. L.; Dronskowski, R. Crystal orbital hamilton population (COHP) analysis as projected from plane-wave basis sets. *J. Phys. Chem. A* **2011**, *115* (21), 5461−5466.
(44) Henkelman, G.; Uberuaga, B. P.; Jónsson, H. A climbing image nudged elastic band method for finding saddle points and minimum energy paths. *J. Chem. Phys.* **2000**, *113* (22), 9901−9904.
(45) Sundararaman, R.; Letchworth-Weaver, K.; Schwarz, K. A.; Gunceler, D.; Ozhabes, Y.; Arias, T. A. JDFTx: Software for joint density-functional theory. *SoftwareX* **2017**, *6*, 278−284.
(46) Sundararaman, R.; Goddard, W. A. The charge-asymmetric nonlocally determined local-electric (CANDLE) solvation model. *J. Chem. Phys.* **2015**, *142* (6), No. 064107.
(47) Letchworth-Weaver, K.; Arias, T. A. Joint density functional theory of the electrode-electrolyte interface: Application to fixed electrode potentials, interfacial capacitances, and potentials of zero charge. *Phys. Rev. B* **2012**, *86* (7), No. 075140.
(48) Yang, P.; Zhao, Z. J.; Chang, X.; Mu, R.; Zha, S.; Zhang, G.; Gong, J. The Functionality of surface hydroxy groups on the selectivity and activity of carbon dioxide reduction over cuprous oxide in aqueous solutions. *Angew. Chem., Int. Ed. Engl.* **2018**, *57* (26), 7724−7728.
(49) Liu, J.; Sun, L.; Sun, Y.; Sun, J.; Pan, Y.; Xu, M.; Lang, Y.; Zhai, D.; Deng, W.; Li, Y.; Yang, L. Theoretical insights into lanthanide rare earth single-atom catalysts for electrochemical CO_2 reduction. *J. Mater. Chem. A* **2024**, *12* (26), 16183−16189.
(50) Pei, J.; Wang, T.; Sui, R.; Zhang, X.; Zhou, D.; Qin, F.; Zhao, X.; Liu, Q.; Yan, W.; Dong, J.; Zheng, L.; Li, A.; Mao, J.; Zhu, W.; Chen, W.; Zhuang, Z. N-Bridged Co−N−Ni: new bimetallic sites for promoting electrochemical CO_2 reduction. *Energy Environ. Sci.* **2021**, *14* (5), 3019−3028.
(51) Huang, Y.; Nielsen, R. J.; Goddard, W. A., III Reaction mechanism for the hydrogen evolution reaction on the basal plane sulfur vacancy site of MoS_2 using grand canonical potential kinetics. *J. Am. Chem. Soc.* **2018**, *140* (48), 16773−16782.
(52) Jinnouchi, R.; Anderson, A. B. Electronic structure calculations of liquid-solid interfaces: Combination of density functional theory and modified Poisson-Boltzmann theory. *Phys. Rev. B* **2008**, *77* (24), No. 245417.
(53) Gunceler, D.; Letchworth-Weaver, K.; Sundararaman, R.; Schwarz, K. A.; Arias, T. A. The importance of nonlinear fluid response in joint density-functional theory studies of battery systems. *Model. Simul. Mater. Sci. Eng.* **2013**, *21* (7), No. 074005.

https://doi.org/10.1021/acs.chemmater.4c02106
Chem. Mater. 2025, 37, 1382−1392